

# Thermally-Induced Degradation in PM6:Y6-based Bulk Heterojunction Organic Solar Cells

Shahidul Alam<sup>1,\*</sup>, Haya Aldosari<sup>1,2</sup>, Christopher E. Petoukhoff<sup>1</sup>, Xinyu Jiang<sup>3,4</sup>, Tomáš Váry<sup>5</sup>, Wejdan Althobaiti<sup>1</sup>, Maryam Alqurashi<sup>1</sup>, Hua Tang<sup>1</sup>, Jafar I. Khan<sup>1,9</sup>, Vojtech Nádaždy<sup>6,7</sup>, Peter Müller-Buschbaum<sup>3,4</sup>, Gregory C. Welch<sup>7</sup>, Frédéric Laquai<sup>1,\*</sup>

<sup>1</sup>King Abdullah University of Science and Technology (KAUST), KAUST Solar Center (KSC), Physical Sciences and Engineering Division (PSE), Material Science and Engineering Program (MSE), Thuwal 23955-6900, Kingdom of Saudi Arabia

<sup>2</sup>Department of Physics, College of Science, Imam Abdulrahman Bin Faisal University, P.O. Box 383, 31113, Dammam, Saudi Arabia

<sup>3</sup>Heinz Maier-Leibnitz Zentrum (MLZ), Technical University of Munich, Lichtenbergstr. 1, 85748 Garching, Germany

<sup>4</sup>Technical University of Munich, TUM School of Natural Sciences, Department of Physics, Chair for Functional Materials, James-Frank-Str. 1, 85748 Garching, Germany

<sup>5</sup>Faculty of Electrical Engineering and Information Technology, Slovak University of Technology, 812 19 Bratislava, Slovak Republic

<sup>6</sup>Institute of Physics, Slovak Academy of Sciences, Dúbravská cesta 9, 845 11 Bratislava, Slovak Republic

<sup>7</sup>Centre for Advanced Material Application, Slovak Academy of Sciences, Dúbravská cesta 9, 845 11 Bratislava, Slovak Republic

<sup>8</sup>Department of Chemistry, University of Calgary, 731 Campus Place N.W., Canada

<sup>9</sup>Department of Physics, School of Natural Sciences, University of Hull, HU6 7RX, United Kingdom (UK)

Thermally-induced degradation of organic photovoltaic devices hinders the commercialization of this emerging PV technology. Thus, a precise understanding of the origin of thermal device instability, as well as identifying strategies to circumvent degradation is of utmost importance. Here, we investigate thermally-induced degradation of state-of-the-art PBDB-T-2F (PM6):BTP (Y6) bulk heterojunction solar cells at different temperatures and reveal changes of their optical properties, photophysics, and morphology. The open-circuit voltage and fill factor of thermally degraded devices are limited by dissociation and charge collection efficiency differences, while the short-circuit current density is only slightly affected. Energy-resolved electrochemical impedance spectroscopy measurements reveal that thermally degraded samples exhibit a higher energy barrier for the charge-transfer state to charge-separated state conversion. Furthermore, the field dependence of charge generation, recombination, and extraction are studied by time-delayed collection field and transient photocurrent and photovoltage experiments, indicating significant bimolecular recombination limits device performance. Finally, drift-diffusion simulations of the devices' current-voltage characteristics using the spectroscopically obtained kinetic parameters and process yields are shown to reproduce the experimentally measured device photocurrent-voltage dependence.

**Corresponding authors:** Shahidul Alam, Frédéric Laquai

**Emails:** [shahidul.alam@kaust.edu.sa](mailto:shahidul.alam@kaust.edu.sa), [frederic.laquai@kaust.edu.sa](mailto:frederic.laquai@kaust.edu.sa)

This is the peer reviewed version of the following article: S. Alam, H. Aldosari, C. E. Petoukhoff, T. Váry, W. Althobaiti, M. Alqurashi, H. Tang, J. I. Khan, V. Nádaždy, P. Müller-Buschbaum, G. C. Welch, F. Laquai, Thermally-Induced Degradation in PM6:Y6-Based Bulk Heterojunction Organic Solar Cells. *Adv. Funct. Mater.* 2024, 34, 2308076, which has been published in final form at <https://doi.org/10.1002/adfm.202308076>. This article may be used for non-commercial purposes in accordance with Wiley Terms and Conditions for Use of Self-Archived Versions. This article may not be enhanced, enriched or otherwise transformed into a derivative work, without express permission from Wiley or by statutory rights under applicable legislation. Copyright notices must not be removed, obscured or modified. The article must be linked to Wiley's version of record on Wiley Online Library and any embedding, framing or otherwise making available the article or pages thereof by third parties from platforms, services and websites other than Wiley Online Library must be prohibited.

# 1. Introduction

In recent years, breakthroughs in organic semiconductor material design, structure optimization, and charge carrier transport layer modification have led to substantially increased power conversion efficiencies (PCEs) of organic solar cells (OSCs) beyond 18% [1-7]. Due to the possibility of their high throughput processing/manufacturing, lightweight, semi-transparency, ability to be rendered flexible, and high form factor, OSCs have attracted significant attention [8-15] as technology to provide cheap and clean electricity to accelerate the world's energy transition. Enhancing the stability of OSCs is of utmost importance for commercialization [16-20], since lifetimes of hundreds of hours found for state-of-the-art high-performance OSCs are insufficient [21] for practical applications. Different extrinsic stressors, including oxygen, moisture, temperature, and radiation, have been shown to limit the stability and facilitate the degradation of OSCs in real-world operating conditions [22-25]. Unwanted evolution of the active layer morphology and diffusion of the charge carrier transport layer and electrode materials into the photoactive layer occur even in the absence of external stressors. Ambient oxygen and water can penetrate an entire device, leading to the degradation of its electrodes, interlayers, and photoactive layers, both chemically and physically [26]. As OSCs work in the presence of light, light-induced degradation poses an intrinsic limitation to the device stability during operation, since it facilitates degradation processes [27]. Component de-mixing in the bulk-heterojunction (BHJ) structure is enhanced at elevated temperatures but does exist even at ambient temperatures because of the frozen non-equilibrium morphology of many bulk heterojunctions [28]. Consequently, revealing the mechanism of thermally-induced degradation along with any photo-degradation processes has gained importance [29-33]. Under continuous illumination, OSCs usually exhibit a steep efficiency decrease within a relatively short time period, termed "burn-in", followed by a more steady loss of efficiency over a more extended period of time [34-36].

OSC performance is known to be dependent on the energetic landscape and nanoscale morphology of the BHJ, which both control charge generation, transport, and carrier collection. However, optimized blend morphologies are generally susceptible to temperature-induced aging, since the active layer morphology evolves towards the thermodynamically most stable state, which can lead to significant de-mixing, decreasing the overall donor-acceptor (D-A) interfacial area and thus the device performance [37, 38]. While the photo and thermal stability of fullerene-based solar cells have been extensively investigated over the past few decades [39], investigations on the stability of non-fullerene-based OSCs are still in their

early stages [40-43]. Many highly efficient non-fullerene acceptors (NFAs)-based OSCs are very sensitive to temperature changes, and the thermal instability of the BHJ limits outdoor applications [44].

Generally, non-optimal morphologies and processes such as charge recombination limit the overall device performance, namely, the device PCE. Thus, understanding what determines the performance is critical to addressing the limitations [45-47]. Limited reports exist on how thermal annealing affects the segregation of photoactive D-A materials and the interface to the transport layers or electrodes in OSCs. Furthermore, changes in the energetics of D-A blends induced by thermal annealing have not been entirely understood. Although water and oxygen in the device can be discharged during solution-processing of transport layers and during annealing, structural and morphological alterations cannot be avoided and can lead to a decreased device performance.

This study reveals the impact of thermal degradation of state-of-the-art PM6:Y6-based OSCs in a nitrogen environment at different annealing temperatures. The degradation mechanism has been identified as an interfacial change in the device due to morphological changes in the photoactive layer. The as-cast device showed a short-circuit current density ( $J_{SC}$ ) of 23.69 mA.cm<sup>-2</sup>, an open-circuit voltage ( $V_{OC}$ ) of 827 mV, and a fill factor (FF) of 66 %, which yields a PCE of 12.83 %. Upon thermal annealing at 80 °C, an initial increase of the device was observed, followed by a significant reduction of the  $V_{OC}$ , FF, and PCE, with only minor changes of the  $J_{SC}$ . The photoluminescence quenching efficiency (PLQE) confirmed that exciton quenching remained more significant in all devices in line with minor photocurrent changes. The  $V_{OC}$  and FF losses of the thermally-aged OSCs can be explained by reduced charge carrier mobility, especially hole mobility, reduced charge extraction, and increased non-radiative charge recombination. From grazing-incidence wide-angle X-ray scattering (GIWAXS) measurements, we inferred that the unfavorable phase separation at the D-A interface limited the charge extraction. While the blend annealed at higher temperatures exhibited increased crystallinity, vertical charge transport was limited owing to a fibrillar-like structure, as further confirmed by atomic force microscopy (AFM). Using energy-resolved electrochemical impedance spectroscopy (ER-EIS), we determined the density of states (DOS) of neat materials and D-A blends. The results show that the voltage drop is due to energy shifts in the blend occurring upon annealing, creating an energetic barrier at the donor-acceptor interface and limiting the charge transfer state to charge-separated state conversion. Transient photovoltage and photocurrent experiments and time-delayed collection field (TDCF) measurements were used to examine the device's charge generation and recombination processes. Both techniques reveal the changes in the device's charge generation and recombination dynamics after annealing at different temperatures. Coupled optical-

electrical device simulations were conducted to fit the device's current voltage (I-V) using SETFOS (FLUXiM) to support our conclusions.

## 2. Results and discussion

### 2.1. Photovoltaic properties

The chemical structures and energy levels of the materials and the device architecture are shown in **Figure 1 (a,b,c)**. BHJ OSC devices based on PM6:Y6 as a photoactive layer were prepared in the inverted device architecture, that is, glass/ITO/ZnO/PM6:Y6/MoO<sub>3</sub>/Ag. Further details can be found in the experimental section. **The devices were annealed on a hotplate inside a glovebox for 10 minutes at different temperatures, while as-cast (non-annealed) devices served as a reference.**

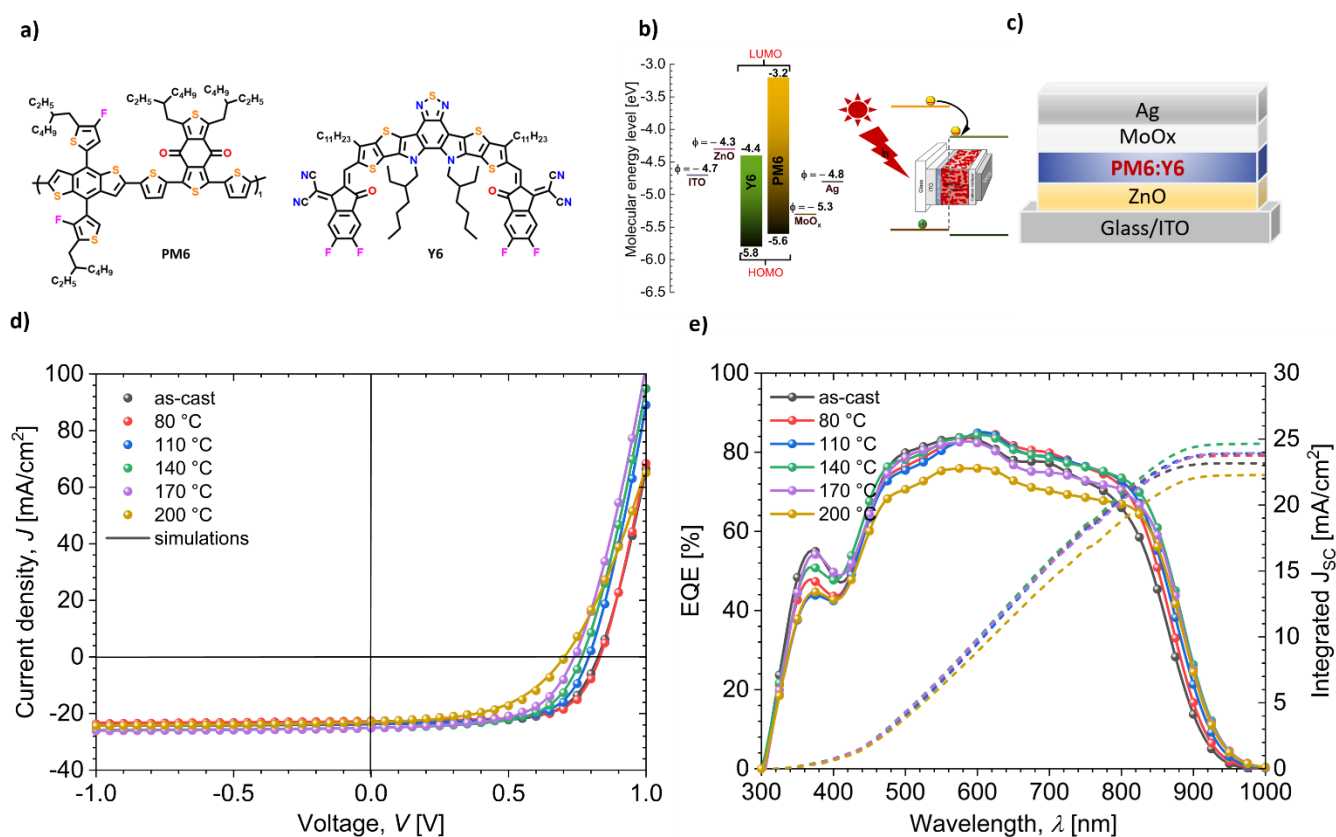


**Figure 1:** (a) Schematic representation of the chemical structures of PM6 and Y6, (b) energetics of donor and acceptor determined by ER-EIS measurements and work functions from the literature [48] of transport layer and electrode materials, and (c) representation of the inverted polymer solar cell architecture, (d) current density-voltage ( $J$ - $V$ ) characteristics, (e) external quantum efficiency (EQE), and integrated  $J_{sc}$  calculated from the EQE measurements of the PM6:Y6 OSCs as-cast and annealed at different temperatures.

Current density-voltage ( $J$ - $V$ ) in dark and under illumination were measured, as well as the devices' external quantum efficiency (EQE). **Figure 1 (d,e)** shows the  $J$ - $V$  characteristics under one sun

illumination (AM1.5 G at 100 mW/cm<sup>2</sup>), the spectral (EQE) response, and the calculated J<sub>SC</sub> of the devices as determined from the EQE for correction of the power conversion efficiency. The calculated J<sub>SC</sub> values are in line with those measured under solar-like illumination. The reference device (as-cast) exhibited diode-like behavior with a rectification ratio of more than two orders of magnitude when comparing the current density under reverse and forward bias, as shown in **Figure S1** in the supporting information (SI). With increasing post-processing annealing temperature, the photocurrent density (J<sub>SC</sub>) increased and reached a maximum for devices annealed at 140 °C, followed by a gradual decrease at higher temperatures (**Table 1**). **The statistical evaluation of all photovoltaics parameters as a function of annealing temperatures is shown in Figure S2.**

**Table 1:** Photovoltaic parameters corresponding to the OSCs as-cast annealed at varying temperatures (EQE corrected). Here short circuit current is J<sub>SC</sub>; open circuit voltage is V<sub>OC</sub>; fill factor is FF, power conversion efficiency is η, series resistance is R<sub>s</sub>, and parallel resistance is R<sub>p</sub>. The samples were annealed at different temperatures for 10 min.

| Annealing temperature | J <sub>sc</sub> (mA/cm <sup>2</sup> ) | J <sub>sc</sub> (EQE) (mA/cm <sup>2</sup> ) | V <sub>oc</sub> (mV) | FF (%)    | η (%)        | η (EQE) (%)  | R <sub>s</sub> (Ω) | R <sub>p</sub> (Ω) |
|-----------------------|---------------------------------------|---|----------------------|-----------|--------------|--------------|--------------------|--------------------|
| As-cast               | 23.69                                 | 23.16                                       | 827                  | 66        | 12.83        | 12.64        | 5.38               | 843                |
| <b>80 °C</b>          | <b>22.60</b>                          | <b>23.75</b>                                | <b>833</b>           | <b>70</b> | <b>13.08</b> | <b>13.84</b> | <b>5.32</b>        | <b>731</b>         |
| 110 °C                | 23.38                                 | 23.92                                       | 792                  | 67        | 12.44        | 12.69        | 4.16               | 479                |
| 140 °C                | 25.12                                 | 24.66                                       | 769                  | 61        | 11.68        | 11.56        | 3.90               | 479                |
| 170 °C                | 23.90                                 | 23.94                                       | 742                  | 58        | 10.73        | 10.30        | 3.69               | 333                |
| 200 °C                | 22.87                                 | 22.29                                       | 705                  | 53        | 8.60         | 8.33         | 5.54               | 243                |

Lastly, drift-diffusion simulations of the devices' J-V characteristics using the spectroscopically measured kinetic parameters (see section 3 in SI) and process yields are shown to match the experimentally measured device J-V dependence. The reconstructed J-V curves of the OSCs are depicted in **Figure 1d** as solid lines overlaying the experimental J-V characteristics. All devices show excellent agreement between simulated and experimentally measured J-V characteristics.

However, the changes in J<sub>SC</sub> with increasing annealing time were relatively small compared to the changes in V<sub>OC</sub> and FF. Coupled optical drift-diffusion simulations of the devices' J-V characteristics were conducted to fit the experimentally measured J-V curves (see **Figure S3** and **Table S1** in the SI). The simulations gave insight into the mechanisms that could cause the changes in the FF, V<sub>OC</sub>, and J<sub>SC</sub> – each arising predominantly from changes in the mobility, energetics, and charge generation efficiency, respectively (**Figure S4**). In order to experimentally validate the origin of the changes in the devices'

figures-of-merit following thermal annealing, charge generation, and recombination processes, morphology and energetics were investigated for the same set of devices.

## 2.2. Optical properties

The thin film absorbance spectra of the pristine donor polymer and NFA materials and their respective blends were measured; the absorbance spectra of pristine samples are shown in **Figures S5 and S6**, and the blend is shown in **Figure 2a**. The films were annealed at five different temperatures, and their absorbance spectra were then compared with those obtained for as-cast films. The absorption of the pristine donors ranges from 500 nm to 700 nm with two peaks at 580 nm and 625 nm, indicated by the dashed lines as  $A_{0-1}$  and  $A_{0-0}$  absorption bands (**Figure S5**). The lowest energy absorption feature for the pristine acceptor has maximum at 855 nm with two vibronic replicas at 740 nm ( $A_{0-1}$ ) and 680 nm ( $A_{0-2}$ ), respectively [49] (**Figure S6**). The peak wavelength positions remain unchanged for both the pristine donor and acceptor upon thermal annealing of the films. However, there is a slight difference in the intensity of the lowest energy absorption bands observed for the pristine acceptor upon annealing. In the case of pristine donors, there is a significant change when going from as-cast to 110 °C annealed films, while the absorption remains unaltered for higher temperatures. The absorption spectra of the blends clearly show three bands originating from the donor and acceptor materials and a blue shift for the acceptor absorption with temperature (**Figure 2a**). The films annealed at temperatures beyond 140 °C exhibit increased absorbance across the entire spectral range. Annealing at higher temperatures facilitates the evolution of a more crystalline arrangement of molecules in the films. Generally, the annealing process at elevated temperatures influences the material's morphology and surface properties. The phase separation between donor-acceptor changes upon thermal annealing due to changes in domain sizes. The observed alterations in structural and morphological properties can influence the film's light scattering and optical properties, leading to increased absorbance. Furthermore, reorientation of molecules within the film occurring at higher temperatures can change the absorbance of the films.

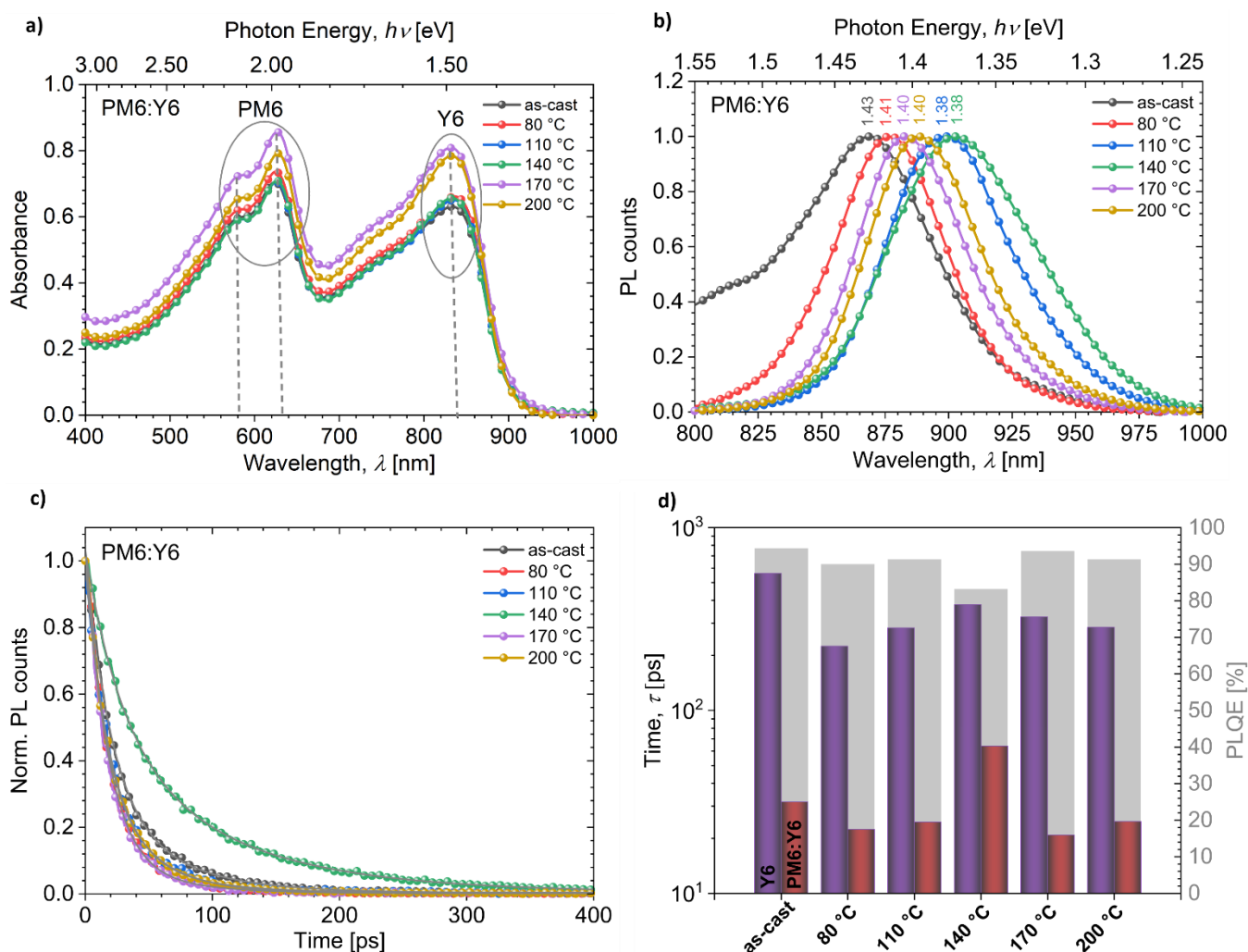


**Figure 2:** Optical properties of pristine PM6:Y6 blend films upon thermal annealing. (a) Absorbance, (b) time-resolved photoluminescence (TRPL) spectra integrated over the first 3-4 ps, and (c) TR-PL transients tracked at the emission maximum of Y6 upon optical excitation at 500 nm, (d) PL lifetime of neat Y6 and PM6 (left axis) and the calculated PLQE (right axis).

Time-resolved photoluminescence (TRPL) measurements on pristine and photoactive blend films were used to track the transition from excitonic states to CT states. A red shift of the TRPL spectra for pristine PM6 can be observed with annealing. A second emission band is visible at 750 nm, as shown in **Figure S7**. The pristine acceptor shows slightly different features after annealing, as shown in **Figure S8**. The redshift of the PL spectra of the annealed acceptor samples compared to the as-cast (non-annealed) sample can be attributed to the aggregation of the molecules leading to changes in intermolecular interaction and, thus, differences in packing. More specifically, a red shift is observed between as-cast and 80 °C to 110 °C. The peak then blue shifts from 110 °C to 140 °C, before red shifting again at higher annealing temperatures (**Figure S9**). The relative emission for the as-cast blend is higher, from 800 to 850 nm

compared to annealed samples and quenched once they are annealed (**Figure 2b**). The blend annealed at 140 °C exhibits the most significant changes caused by the presence of the acceptor (Y6). Qian *et al.* systematically studied the glass transition temperature ( $T_g$ ) of several BTP-based NFAs and developed a compound structure- $T_g$  framework using the Gordon-Taylor relation [50]. Interestingly, the glass transition temperature  $T_g$  for Y6 was observed at  $102 \pm 1$  °C, where a change can also be observed from the PL spectra. However, spectral shifts occurred up to 140 °C, as seen for the blends' PL spectra, likely due to the glass transition temperature of the donor PM6 at approximately 135 °C. Clearly, the changes are significant for the sample heated to 140 °C. An overview of the peak positions for the pristine and blend samples is shown in **Figure S9** in SI.

To study the exciton quenching efficiency of the blends, we compared the TRPL transients of pristine materials (see **SI Figure S10** and **Figure S11**) and photoactive blend thin films coated on quartz substrates following optical excitation at 500 nm. The TRPL transients of Y6 and blends were tracked at their peak emission wavelength, dominated by the acceptor's emission, as depicted in **Figure 2(b)**. The decays (see **Figure 2(c)**) were parameterized by a double-exponential decay function, and the amplitude-averaged PL lifetimes were determined (**Table S2**, in SI) as reported previously and shown in **Figure 2(d)** (left axis) [51, 52]. The photoluminescence quenching efficiency (PLQE) was estimated using the relation  $1 - \tau_{\text{blend}}/\tau_{\text{pristine}}$ , where  $\tau_{\text{blend}}$  and  $\tau_{\text{pristine}}$  are the PL lifetimes of the blend and pristine Y6 thin films, respectively. All samples exhibited PLQEs around 90%, as shown on the right axis of **Figure 2(d)**. The TRPL spectra pristine PM6, pristine Y6, and blend films annealed at different temperatures are shown in **SI Figures S12**, **S13**, and **S14**, respectively.

### 2.3. Structural and morphological properties

GIWAXS measurements were used to determine the crystallite structure in the thin films after annealing the PM6:Y6 blends at various temperatures. **Figure 3(a)**, shows the 2D GIWAXS data of PM6:Y6 blends, and the corresponding out-of-plane (OOP) / in-plane (IP) line profiles are given in **Figure 3(b)**. All the samples had a face-on dominated crystal orientation with the (100) peak located at  $0.27$  [ $\text{\AA}^{-1}$ ] in the in-plane (IP) direction and (010) peak located at  $1.73$  [ $\text{\AA}^{-1}$ ] in the out-of-plane (OOP) direction. The details of the peak position, the estimated crystal stacking distance, as well as the crystal size calculated from Scherrer equation, are listed in **SI, Table S3**. There is no noticeable difference between the as-cast sample and the 80 °C annealing treatment from GIWAXS data. In the OOP direction, the (010) peak remained at  $1.73$  [ $\text{\AA}^{-1}$ ] for all samples, suggesting a constant  $\pi$ - $\pi$  stacking distance. However, the (010) crystal size shranked from 1.95 nm for the as-cast sample to 1.82 nm, when the annealing temperature was 110 °C,

while an increase in size (2.02 nm) was observed after 140 °C annealing. For IP (100) peaks, the peak slightly shifts from 0.27 [ $\text{\AA}^{-1}$ ] to 0.28 [ $\text{\AA}^{-1}$ ], indicating a decrease in stacking distance. Notably, the corresponding crystal size increased when the annealing temperature was  $\geq 110^\circ\text{C}$ . This suggests the growth of the (100) crystallinity by annealing treatment  $\geq 110^\circ\text{C}$ . Furthermore, the isotropic crystallinity size located at 1.46 [ $\text{\AA}^{-1}$ ] in the whole azimuthal range increased to the highest value at 110 °C, suggesting the highest isotropic crystallinity contribution among all annealed samples.

To investigate the orientation distribution of the (100) crystal packing, we executed circular cuts data from  $-90^\circ$  to  $+90^\circ$  in a  $q$  range from 0.2 to 0.4  $\text{\AA}^{-1}$  as shown in **Figure 3c** [53]. In order to get a better view, the data from  $0^\circ$  to  $90^\circ$  are shown in **Figure S15**. The arc higher than  $45^\circ$  which is highly related to the face-on crystallinity orientation. The sample annealed at 110 °C showed the lowest crystallite distribution among all samples in the face-on-dominated region. The 140 °C film showed higher face-on orientation distribution but was still lower than the as-cast and 80 °C samples. With further increase in annealing temperature, the face-on dominated orientation became more pronounced in the samples annealed at 170 °C and 200 °C, respectively. Face-on crystallinity is beneficial for the charge transport pathway in the active layer only if the donor and acceptor are intermixed well. Above all, we have found the sample annealed at 110 °C showed the lowest face-on crystallinity while having the highest isotropic crystallinity, suggesting the charge transport pathway is more favorable. Although the samples annealed at temperatures above 110 °C showed an increase in the face-on crystallinity orientation, since the device performance became worse from J-V measurements, this suggests an unfavorable phase separation in the donor and acceptor blend.

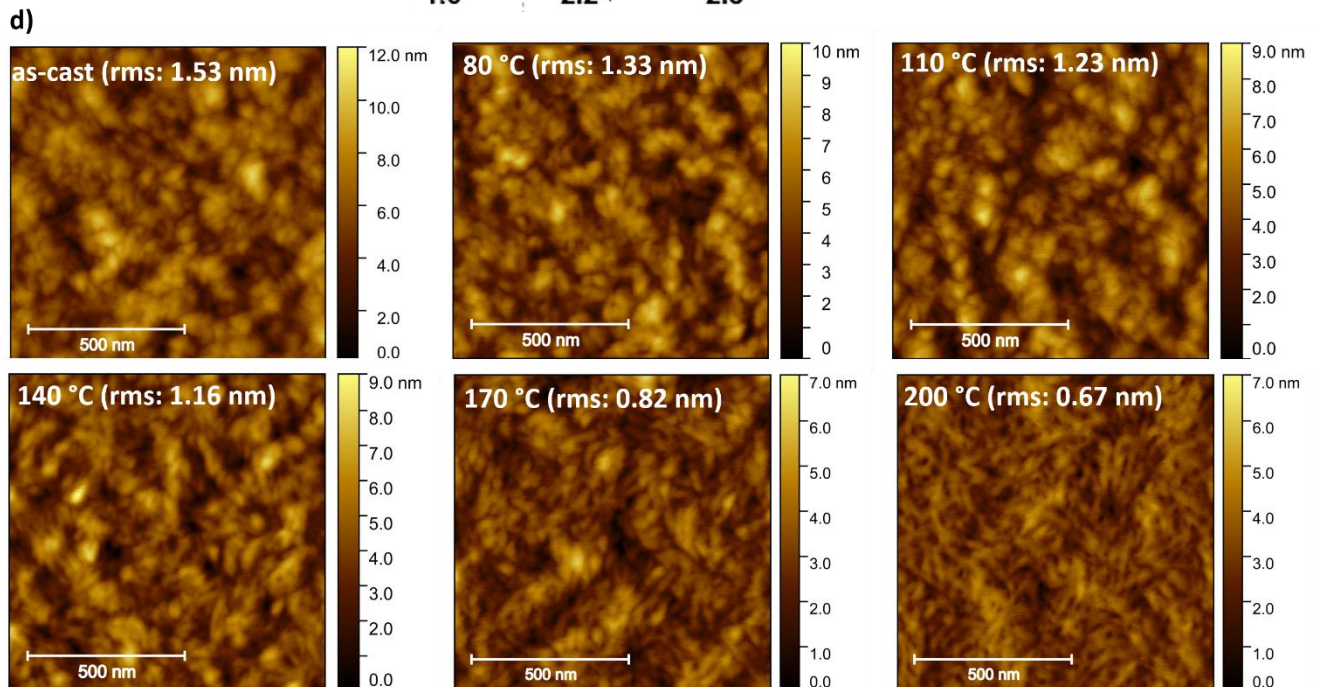
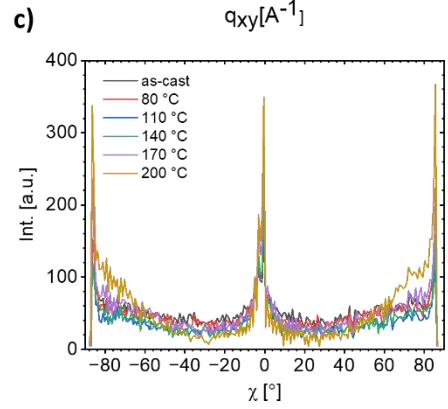
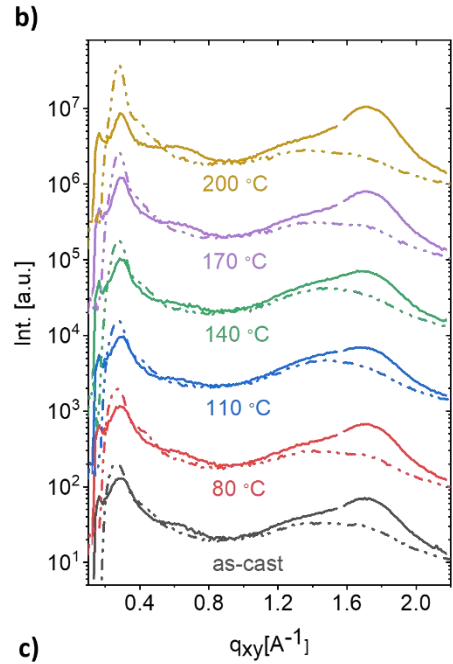
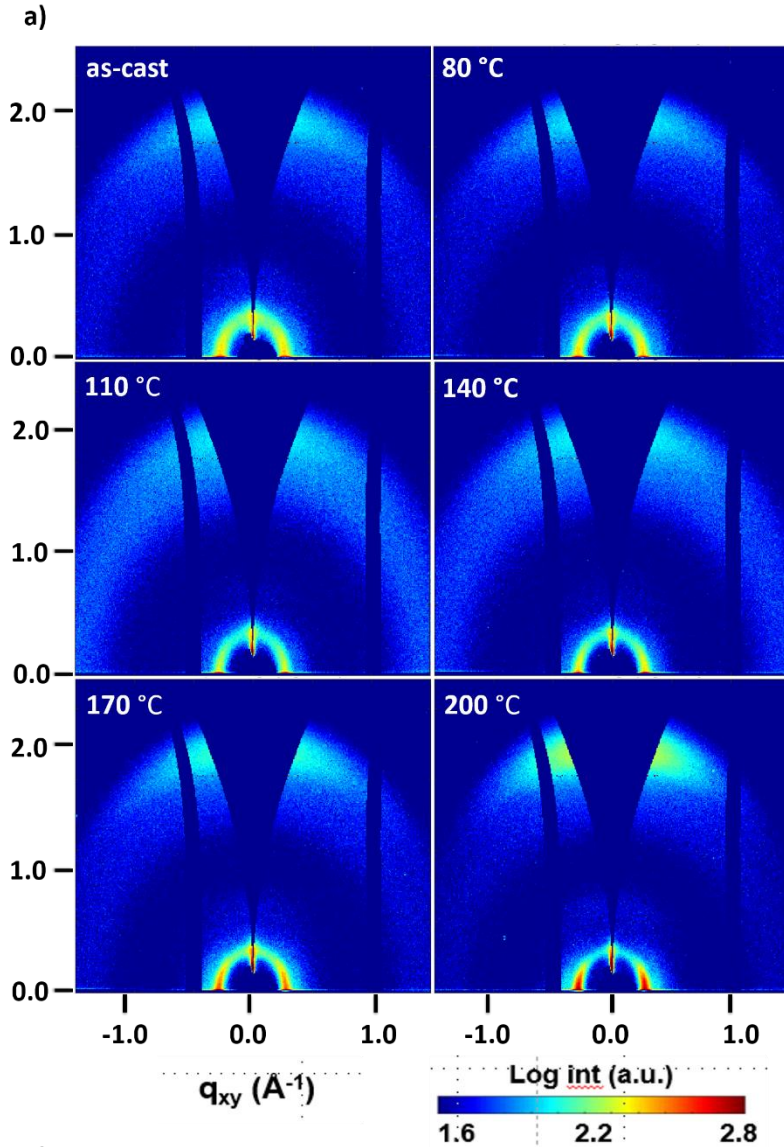


**Figure 3:** (a) 2D GIWAXS data for PM6:Y6 blends annealed at different temperatures as indicated. (b) Scattering line profiles in the out-of-plane (OOP, solid line) and in-plane (IP, dash line) direction and, c) azimuthal cut (i.e., tube cut,  $\chi$  from  $-90^\circ$  to  $90^\circ$ ) along the (100) peak of the PM6:Y6 blends annealed at different temperatures, respectively. (d) Atomic force microscopy (AFM) images of PM6:Y6 blends annealed at different temperatures.

To acquire a deeper understanding of the morphological changes, AFM was used to investigate the topography of the films' surface. **Figure 3d** shows the topography images of PM6:Y6 blends that were annealed at different temperatures. Thermal annealing of the blend films did not result in significant changes up to 140 °C, while thermal annealing at or above 170 °C clearly showed morphological changes. In particular, crystallization was developed for the samples annealed at higher temperatures, which might lead to unfavorable molecular mobility in a temperature range close to the transition temperature of PM6. By summarizing optical and structural investigations and considering the morphological changes, we could state that the device annealed at a higher temperature is unfavorable for vertical charge transport due to the fibrillary-like structure.

#### 2.4. Energetics of pristine and blend films

ER-EIS is a sophisticated method that allows determining the energetic landscape of semiconductor thin films used as active layers in OSCs. Furthermore, information about the DOS can be obtained for pristine and blend films [54, 55]. The DOS of as-cast and thermally-annealed films of pristine PM6, pristine Y6, and PM6:Y6 blends are shown in **Figure 4** and **Figures S16, S17, and S18 in SI**. The linear offsets of the DOS's function are typically assigned to the corresponding band edges. The onset of peaks can be used to determine the energies of the highest occupied molecular orbital (HOMO) and lowest unoccupied molecular orbital (LUMO) and thus to calculate the transport gaps of pristine, as well as of D-A blend films. The DOS for all pristine and blend in linear scale are presented in **SI**, from **Figures S19 to S24**. The intersections of dashed lines with the energy axis determine the onset values of HOMOs and LUMOs of particular films. A summary of HOMO and LUMO values of pristine PM6 and Y6 films as a function of annealing temperature is given in **Table S4**. With regard to the OSC performance, it is important to determine the so-called effective band gap,  $E_{g,eff}$  [54], which is the experimentally-determined energy difference between the HOMO onset of the donor (PM6) and LUMO onset of the acceptor (Y6) in the BHJ photoactive layer. The values of HOMO, LUMO, and  $E_{g,eff}$  obtained on PM6:Y6 as-cast and annealed blends are presented in **Table 2**. There is a gradual decrease of the HOMO energy from  $-5.68$  eV for the as-cast layer to  $-5.85$  eV for the layer annealed at 200 °C. The LUMO energy first increases from  $-4.24$  eV to  $-4.40$  eV after annealing at 80 °C and then gradually decreases with increasing annealing temperature to  $-4.16$  eV for 200 °C. These changes first result in a narrowing of the band gap for the film

annealed at 80 °C from 1.44 eV to 1.30 eV and then to a gradual increase with annealing temperature up to 1.69 eV for 200 °C.

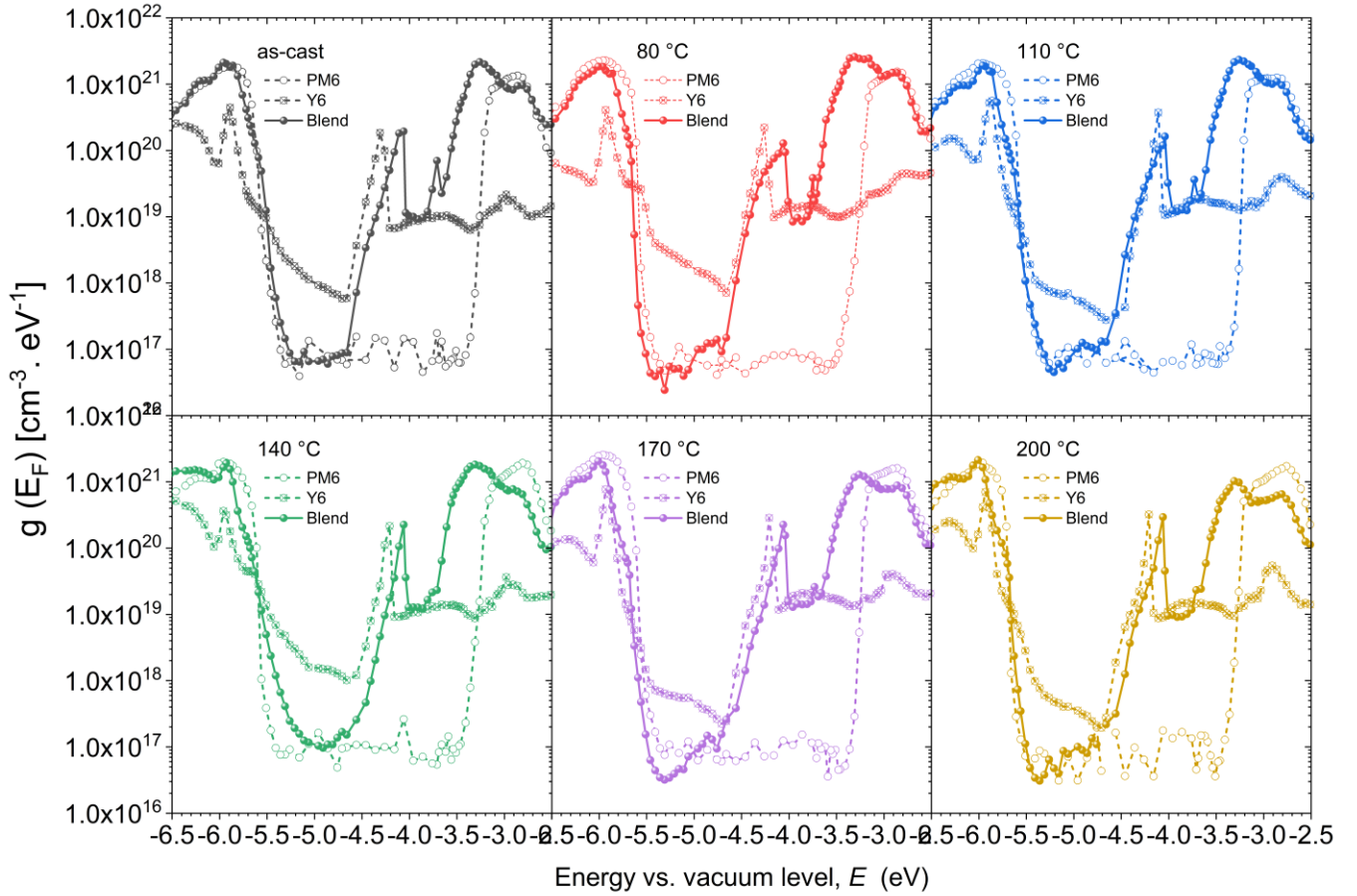


**Figure 4:** Density of states (DOS) function  $g(E_F)$  for the films (pristine PM6, pristine Y6, and PM6:Y6 blend) as-cast and thermally annealed at different temperatures.

As we recently reported,  $E_{g,eff}$ , together with the charge transfer exciton (CTE) energy are important quantities that determine the charge generation yield [54]. The lower limit of the CTE energy in the PM6:Y6 blend layers can be evaluated from the peaks of the PL spectra. CTE-PL energies taken from **Figure 2b** are included in **Table 2** along with the CTE-PL- $E_{g,eff}$  difference, which correlates with the efficiency of the charge generation process. Positive values imply barrier-less charge generation. On the other hand, negative values indicate that the transition from the charge-transfer state to the charge-separated state requires overcoming an energy barrier. A high negative value implies that charge generation is impeded. Looking at the photovoltaic parameters in **Table 1**, we can identify a correlation between changes in the device performance and the CTE-PL- $E_{g,eff}$  difference.

**Table 2:** HOMO energy, LUMO energy, effective band gap,  $E_{g,eff}$ , charge transfer exciton (CTE) energy determined from PL peak position as a lower limit, and difference CTE-PL –  $E_{g,eff}$  of the PM6:Y6 blend layers annealed at different temperatures.

| Annealing temperature | HOMO [eV] | LUMO [eV] | Effective band gap $E_{g,eff}$ [eV] | CTE-PL [eV] | CTE-PL- $E_{g,eff}$ [eV] |
|-----------------------|-----------|-----------|-------------------------------------|-------------|--------------------------|
| as-cast               | – 5.68    | – 4.24    | 1.44                                | 1.43        | – 0.01                   |
| 80 °C                 | – 5.72    | – 4.37    | 1.35                                | 1.41        | 0.06                     |
| 110 °C                | – 5.76    | – 4.28    | 1.48                                | 1.38        | – 0.10                   |
| 140 °C                | – 5.79    | – 4.16    | 1.63                                | 1.38        | – 0.25                   |
| 170 °C                | – 5.84    | – 4.16    | 1.68                                | 1.40        | – 0.28                   |
| 200 °C                | – 5.85    | – 4.16    | 1.69                                | 1.40        | – 0.29                   |

## 2.5. Charge generation and recombination

Next, we studied charge generation, charge carrier recombination, and charge collection of the OSCs annealed at different temperatures. The PAIOS tool from Fluxim was used to measure the transient photocurrent (TPC), transient photo-voltage (TPV), and charge extraction (CE) [56]. The photocurrent density ( $J_{ph}$ ) as a function of the effective voltage ( $V_{eff}$ ) of the OSCs was investigated to reveal the charge generation and extraction mechanism. The exciton dissociation efficiency ( $\eta_{diss} = J_{SC}/J_{sat}$ ) and charge collection efficiency ( $\eta_{coll} = J_{MPP}/J_{sat}$ ) were calculated at short circuit conditions and at the maximum power point, respectively [57].

TPC measurements were performed to understand qualitative differences of the charge carrier transport properties, and the photocurrent decay was monitored after excitation with a 100  $\mu$ s pulse, as shown in **Figure 5 (a)**. The ratio between charge carriers extracted swiftly and those extracted after some delay time became smaller for increasing annealing temperatures. More specifically, the number of trapped charge carriers increased for higher annealing temperatures. The photocurrent decay time under short circuit conditions was one order of magnitude shorter for the as-cast device than for the devices annealed at a higher temperature. This indicates that morphological changes facilitate charge carrier extraction. Noticeably, a clear transition occurred for the devices annealed from 80 °C to 140 °C. The photo-voltage decay dynamics were monitored to estimate the carrier lifetime under open-circuit conditions, as shown in **Figure 5 (b)**. The carrier decay dynamics were parametrized by a single exponential decay function. The as-cast device exhibited an inverse decay rate of 3.3  $\mu$ s, which was substantially shorter than that of the device annealed at 80 °C (4.86  $\mu$ s) and at 110 °C (6.07  $\mu$ s). Moreover, charge extraction was found to be faster for the devices that were annealed at temperatures up to 110 °C, as shown in **Figure 5 (c)**.

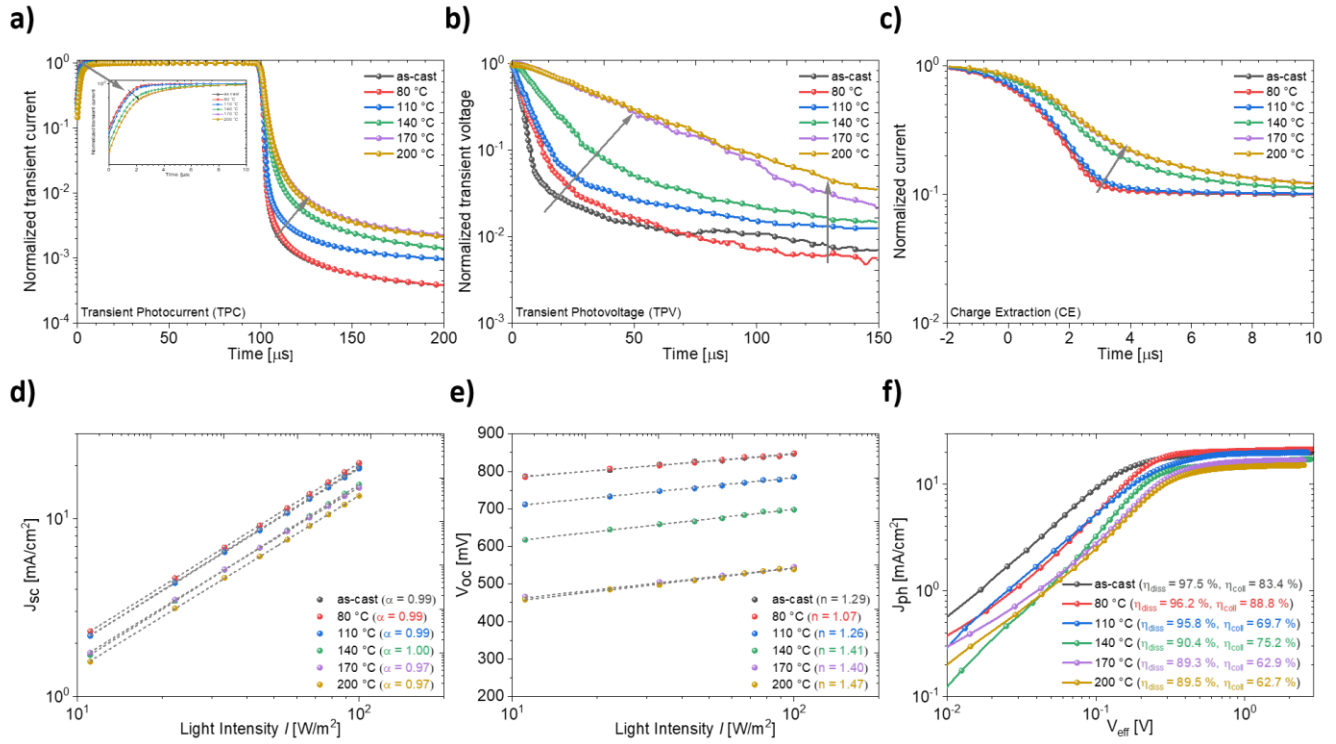


**Figure 5:** Charge generation, recombination, and charge extraction properties. (a) Transient photocurrent, (b) transient photovoltage, (c) charge extraction, (d) short circuit current density vs. light intensity, (e) open circuit voltage vs. light intensity, and (f) photocurrent density as a function of effective voltage.

Light-intensity-dependent J-V measurements were performed to identify differences in the recombination processes that take place in the devices. The bimolecular recombination losses were compared by fitting a simple power law dependence,  $J_{SC} \propto I^\alpha$ , to the short circuit current density vs. light intensity ( $I$ ) dependence, as shown in **Figure 5 (d)**. The slope ( $\alpha$ ) was obtained from the log-log plot; values of  $\alpha$  close to unity imply that non-geminate (bi-molecular) recombination does not significantly impact the short circuit current at the measured light intensities. In fact,  $\alpha$  values obtained for the devices range from 0.97 to 1, specifying negligible non-geminate recombination for all the devices in short circuit conditions [58-60]. Besides, the ideality factors ( $n$ ) were calculated from the  $V_{OC}$  vs. light intensity dependence in a semi-log scale, as shown in **Figure 5 (e)**. The data obeys the relation  $J_{SC} \propto nkT/q \ln(I)$ , where  $k$  is the Boltzmann constant,  $T$  is the temperature, and  $q$  is the elementary charge. Trap-assisted recombination is indicated by  $n$  values deviating from unity [61]. Following this interpretation, the devices annealed above 140 °C appear to be severely limited by trap-assisted charge recombination. Finally, the charge generation and extraction are further analyzed by plotting the photocurrent density ( $J_{ph}$ ) as a function of the effective voltage ( $V_{eff}$ ) as plotted in **Figure 5 (f)**. The  $J_{ph}$  was calculated from the light minus dark J-V

characteristics,  $J_{ph} = J_L - J_D$ , in which  $J_L$  is the current density under illumination and  $J_D$  the current density in the dark [57].  $V_{eff}$  was calculated from the voltage ( $V_0$ ) when  $J_{ph}$  is 0 and the applied bias voltage ( $V_A$ ), that is,  $V_{eff} = V_0 - V_A$ . The dissociation efficiency ( $\eta_{diss} = J_{SC}/J_{sat}$ ) and charge collection efficiency ( $\eta_{coll} = J_{MPP}/J_{sat}$ ) were estimated at short circuit conditions and at the maximum power point, respectively. The as-cast device showed the highest exciton dissociation efficiency of 97.5 %. However, the charge collection efficiency for the device annealed at 80 °C confirmed that some annealing is required to enhance extraction, possibly by changes of the morphology due to donor-acceptor demixing.

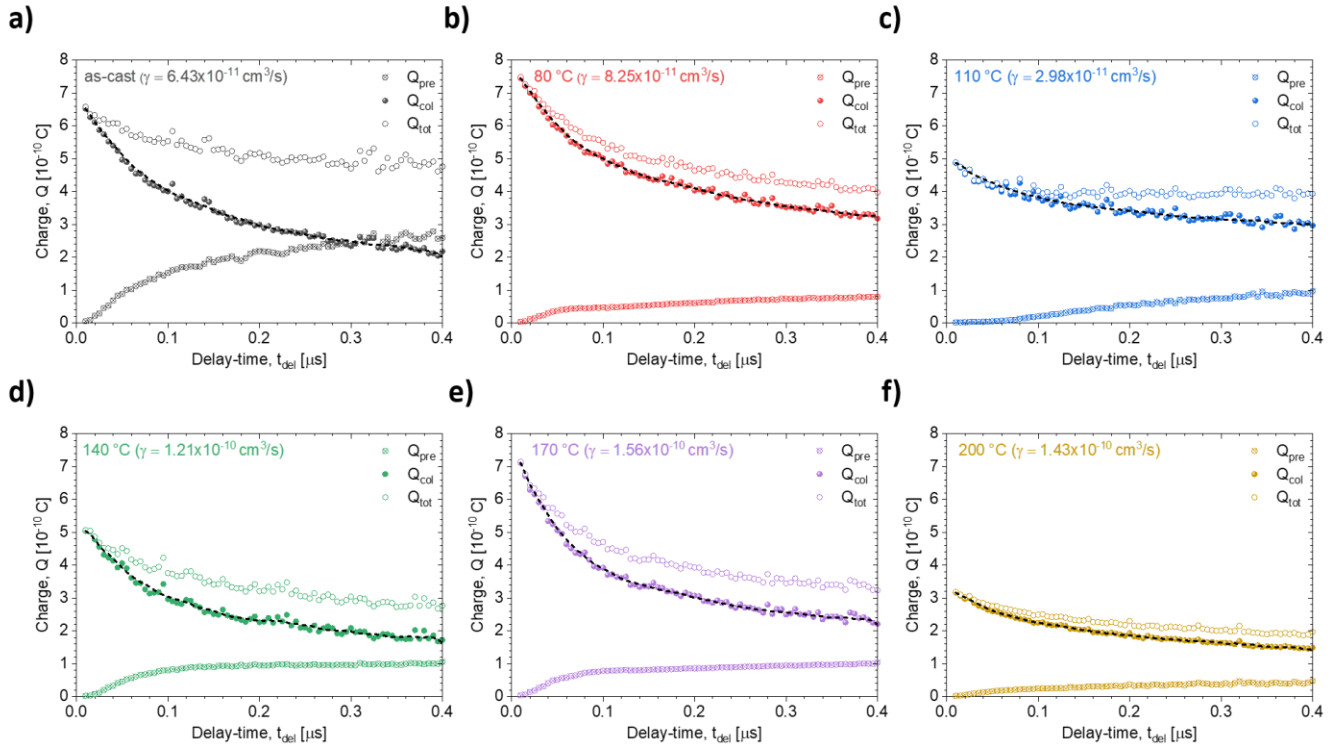


**Figure 6:** Time-delayed collection field measurements for devices annealed at different temperatures. (a) as cast, (b) 80 °C, (c) 110 °C, (d) 140 °C, (e) 170 °C and (f) 200 °C.  $Q_{pre}$  is the amount of charge collected by  $V_{pre}$ , the collected charge  $Q_{col}$ , and the total extracted charge  $Q_{tot}$ .

Time-delayed collection field (TDCF) measurements [62-67] were done using a variable time delay ( $t_{del}$ ) between the photoexcitation (laser pulse) and the application of the collection bias to reveal charge collection in thermally annealed devices. A nanosecond laser pulse with a fluence of  $0.05 \mu\text{J}/\text{cm}^2$  was used to photogenerate charges in the devices. The pre-bias was kept close to  $V_{OC}$  to reduce the impact of the internal electric field, as well as to limit charge extraction during the delay time and prior to collection, ensuring that primarily non-geminate recombination accounts for the bulk of the carrier losses seen from the collected charge. **Figure 6** shows the amount of charge collected by  $V_{pre}$  ( $Q_{pre}$ ), the collected charge  $Q_{col}$ , and the total extracted charge  $Q_{tot}$ .

( $Q_{coll}$ ), and the total extracted charge ( $Q_{tot}$ ) as a function of the time delay. With increased time delay, more charges have already recombined, leaving less charges available for extraction. The recombination rate, namely,  $\gamma$  was extracted based on fits to the following equation [62, 68, 69],

$$q_{coll}(t_d + \Delta t) - q_{coll}(t_d) = -[q_{pre}(t_d + \Delta t) - q_{pre}(t_d)] - \gamma \frac{q_{coll}^2(t_d)}{eAd} \Delta t$$

Here,  $A$  is the device area,  $d$  is the thickness, and  $\gamma$  is the bi-molecular recombination coefficient. The determined bi-molecular recombination coefficient is shown in the respective graph. The bi-molecular recombination coefficients of the as-cast device are  $6.43 \times 10^{-11} \text{ cm}^3/\text{s}$  and  $1.43 \times 10^{-10} \text{ cm}^3/\text{s}$  of the device annealed at  $200 \text{ }^\circ\text{C}$ . The recombination coefficient of the devices annealed at  $140 \text{ }^\circ\text{C}$  or above increased nearly by an order of magnitude.

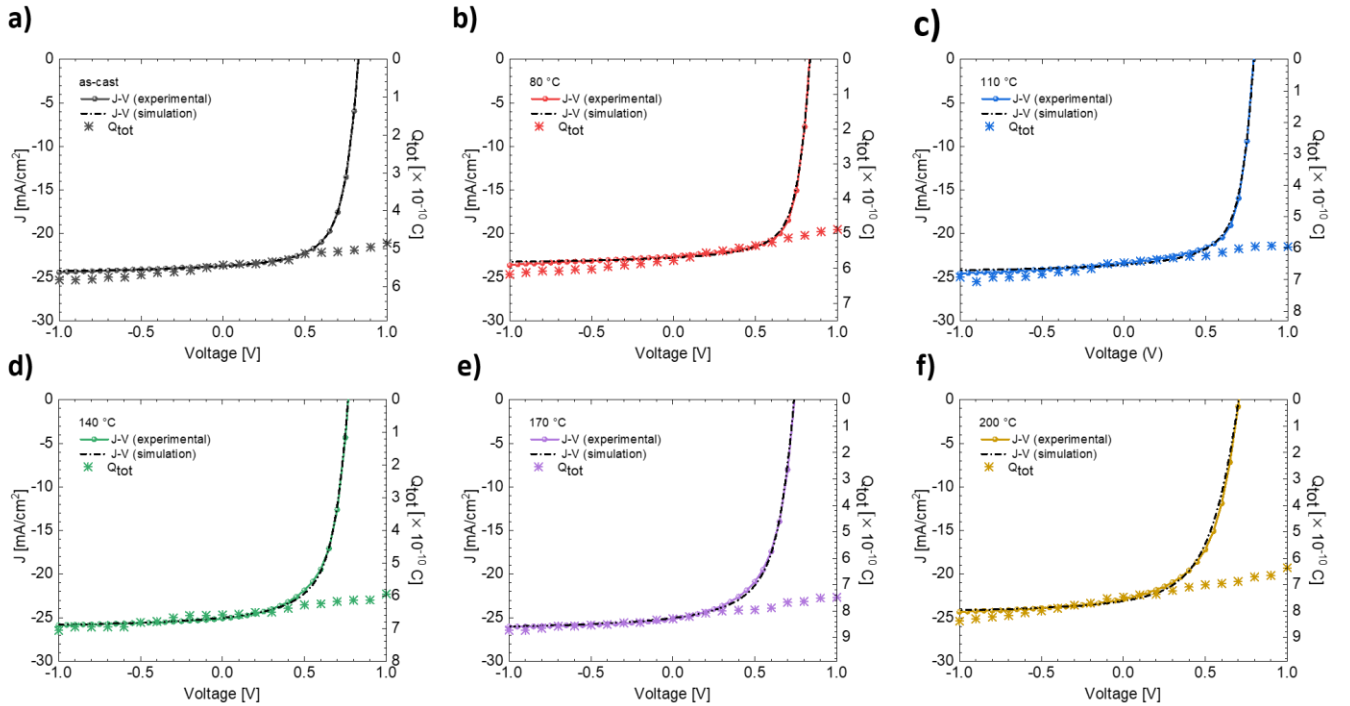


**Figure 7:** The J-V characteristics of OSCs for the as-cast device and annealed devices at different temperatures. The J-V characteristics were simulated with SETFOS device simulator software. The TDCF measurements with the total charge as a function of applied pre-bias overlaid with experimental and simulated J-V characteristics.

Based on the J-V characteristics, the annealing temperature primarily affected the FF of the devices rather than the  $J_{SC}$  and  $V_{OC}$ . In order to reveal the origin of differences in the device's FF after annealing, TDCF measurements were also conducted to evaluate the field dependence of the photo-generated charge carrier yield [70-72]. The total extracted charge was probed as a function of the applied bias during

photoexcitation. The data is shown in **Figure 7**, jointly with the J-V characteristics of the devices for pre-biases in the range of  $-1\text{ V}$  to  $+1\text{ V}$ . In all cases, the collected charge decreases with increasing pre-bias, indicating a component of field-dependent charge generation in the devices. Hence, the FF appears to be mainly governed by field-dependent charge generation in the devices and geminate recombination losses in agreement with the LID-JV measurements.

### **3. Conclusion**

We investigated the effect of thermal annealing on the photophysics and performance of bulk-heterojunction organic solar cells comprised of PM6:Y6 active layer. We observe a performance drop for annealing temperatures around and above  $140\text{ }^{\circ}\text{C}$ . We showed that structural and nanoscale morphological changes affect charge transport and extraction, resulting in substantial decreases of the  $V_{\text{OC}}$  and FF. Furthermore, the blends' energetic landscape is studied, revealing shifts of the energy levels in the BHJ after annealing of the device, confirmed by ER-EIS measurements. These shifts decrease the effective bandgap from  $1.44\text{ eV}$  to  $1.30\text{ eV}$  at  $80\text{ }^{\circ}\text{C}$ , followed by a gradual increase up to  $1.69\text{ eV}$  for the device annealed at  $200\text{ }^{\circ}\text{C}$ . We conclude that an energy barrier exists, which limits the charge-transfer state conversion into charge-separated states. The bimolecular recombination coefficient is found to increase by an order of magnitude for the devices annealed at the highest temperature. Lastly, field-dependent charge generation is found to be limiting the device FF.

## 4. Experimental Section

### *Sample preparation*

All the thin films were prepared either on quartz glass in order to do the optical measurements. In contrast, thin films for electrochemical measurements were processed on ITO/ZnO substrates. Thin films for structural and morphological characterizations were coated either on Si or glass substrates with the same parameters as the active layer for the solar cell devices.

Inverted BHJ solar cells were fabricated with device configuration of ITO/ZnO/PM6:Y6/MoO<sub>3</sub>/Ag. Glass substrates with pre-patterned indium tin oxide (ITO, 16  $\Omega$  sq<sup>-1</sup>) were first cleaned with the dilute detergent solution for 20 min in an ultrasonic bath. Samples were rinsed in flowing deionized water for 5 minutes, followed by a sequential bath of acetone and isopropanol for 15 minutes each. In the next step, these cleaned samples were exposed to UV-ozone plasma cleaning for 15 min. A thin layer of ZnO is spin-coated (4000 rpm) using the ZnO precursor solution. The films were baked at 150 °C for 15 min in the air to give the film thickness of 30–35 nm. The ZnO films were transferred into the glovebox for active layer deposition. The photoactive layer solutions were prepared a day before deposition using polymer PM6 (purchased from 1-material) as donor mix with Y6 as the acceptor (purchased from Organtec Ltd-BETTERCHEM). The donor and acceptors were dissolved in chloroform (CF) at a ratio of 1:1.2 (wt.%), with an overall concentration of 15.11 mg/mL and stirred overnight at a temperature of 40 °C. As a solvent additive, 0.5 vol.% chloro-naphthalene (CN) was added to the host solution. The active layers were spin-coated over the ZnO-coated substrates at 2500 rpm to provide a film thickness of  $\approx$ 90 nm. Afterward, the films were transferred to a thermal evaporator for the evaporation of a 10 nm thick film of MoO<sub>3</sub> followed by a 100 nm thick Ag top electrode with deposition rates of 0.25 and 0.5 Å/s, respectively, through a shadow mask yielding active areas of 0.1 cm<sup>2</sup> in each device.

### *Sample Characterizations*

*Electrical characterization:* J–V measurements of solar cells were performed in the glovebox with a Keithley 2400 source meter and an Oriel Sol3A Class AAA solar simulator calibrated to one sun, AM1.5 G, with a KG-5 silicon reference cell certified by Newport. The EQE measurements were performed at zero bias by illuminating the device with a monochromatic light supplied by a Xenon arc lamp in combination with a dual-grating monochromator.

*Optical characterization:* UV-vis absorption spectra were measured with a Perkin Elmer Lambda 900 UV-vis-NIR absorption spectrometer.

*Device simulation by SETFOS:* 1D numerical drift-diffusion device simulator (Setfos 5.2 from FLUXiM AG) was used to fit the OPV device J–V curves. The optical constants (refractive index and extinction coefficient) were obtained from the literature [73] for PM6:Y6, and from Setfos' materials database for the other materials. The simulations were conducted using the absorption, drift-diffusion, and optimization packages of Setfos. The remaining simulation parameters are included in the Supporting Information section 3 (see **Figures S3, S4** and **Table S1**).

*Time-resolved photoluminescence (TRPL):* The measurements were performed using 710 nm excitation from Coherent (Chameleon) fs laser operating at 80 MHz repetition rate. The thin films were kept in a small nitrogen-filled chamber, and the fluences were in order of 300 nJ/cm<sup>2</sup>. The PL of the samples was collected by an optical telescope (consisting of two plano-convex lenses) and focused on the slit of a spectrograph (PI Spectra Pro SP2300) and detected with a Streak Camera (Hamamatsu C10910) system. The data was acquired in photon counting mode using the Streak Camera software (HPDTA) and exported to Origin Pro 2020 for further analysis.

*Grazing Incidence Wide Angle X-ray Scattering (GIWAXS)*: The GIWAXS measurements were carried out with a SAXSLAB laboratory instrument using a CuK $\alpha$  X-ray source (8.05 keV, 1.54 Å) and a Pilatus 300K detector. The incident angle was 0.2° and the sample-to-detector distance (SDD) was set to 95 mm. The transformation to q-space, radial cuts for the in-plane /out-of-plane analysis, and azimuthal cuts for orientation analysis were processed by the MATLAB-based package GIXSGUI.

*Atomic Force Microscope (AFM)*: Film topography was characterized with a Veeco/Bruker Dimension atomic force microscopy in the tapping mode to gain further insight into possible morphology changes using super sharp tips (TESP-SS). The images were analyzed primarily by Nanoscope v720 software during the measurements and by Gwyddion multiplatform modular free software.

*Platform for all-in-one characterization of solar cells (PAIOS)*: All light intensity dependence measurements on J-V curves, transient photocurrent (TPC), transient photovoltage (TPV), and charge extraction (CE) analyses, experiments were performed using the all-in-one measurement system PAIOS 3.2 (Fluxim). PAIOS 3.2 employs many different device characterization techniques in steady-state and transient modes. A function generator controls the light source: a white LED (rise/fall time 100 ns). A second function generator controls the applied voltage. The current and the voltage of the solar cell are measured with a digitizer. The current is measured *via* the voltage drop over a 20  $\Omega$  resistor or a trans-impedance amplifier, depending on the current amplitude.

*Energy-resolved electrochemical impedance spectroscopy (ER-EIS)*: The density of states (DOS) was characterized by the recently introduced spectroscopic method, energy-resolved electrochemical impedance spectroscopy (ER-EIS) [74, 75]. The DOS function  $g(E)$  in the organic semiconductor is obtained by measuring the charge transfer resistance,  $R_{ct}$ , of a semiconductor/electrolyte interface via the following relation,

$$g(E_F = eU) = \frac{1}{e^2 k_{et} [A] S R_{ct}}$$

$E_F = eU$  is the electrochemical potential adjusted by the external voltage  $U$ ,  $e$  is the elementary charge,  $k_{et}$  is the charge-transfer rate constant,  $[A]$  is the concentration of the electrolyte redox (donor/acceptor) species in the interface region of the solid/liquid contact, and  $S$  is the sample area. The reciprocal value of the  $R_{ct}$  provides direct information about the electronic DOS at the energy-adjusted with an external voltage. The ER-EIS measurements were done in a nitrogen (N<sub>2</sub>) atmosphere glove box employing a standard three-electrode configuration. The electrochemical cells (volume of 200  $\mu$ L) were created by gluing plastic micro cylinders. The solution of 0.1 M TBAPF<sub>6</sub> in acetonitrile was used as the supporting electrolyte. The working electrode's potential with respect to the reference Ag/AgCl electrode was controlled via a potentiostat, and a platinum (Pt) wire served as the counter electrode. The potential recorded for the reference Ag/AgCl electrode can be recalculated to the local vacuum level assuming an Ag/AgCl energy vs. vacuum value of  $-4.66$  eV. Impedance was measured with an impedance/gain-phase analyzer Solartron analytical model 1260. The frequency was set to 0.5 Hz, and the rms value of the AC voltage was 100 mV.

*Time Delayed Collection Field (TDCF)*: The home-built TDCF setup used the second harmonic (532 nm) of an actively Q-switched sub-ns Nd:YVO<sub>4</sub> laser (INNOLAS piccolo AOT) operating at 5 kHz as excitation. To minimize the RC response time (typically a few nanoseconds), a small device area of 1 mm<sup>2</sup> was used. The samples were measured under dynamic vacuum conditions to avoid any degradation. A Keysight S1160A functional generator was used to provide the pre-bias and extraction bias, while a Keysight four-channel digital oscilloscope was used to measure the current response of the device.

*Polarized Light Microscopy*: A Nikon Eclipse optical microscope with a Xenon lamp source was used to image the uniformity of the active layer thin films (SI **Figures S25** and **S26**). The excitation path was polarized in-plane, and a second polarizer (i.e., analyzer) oriented 90° relative to the excitation polarization was used to collect the light reflected from the samples. Films were imaged with a 50× objective.

## Acknowledgments

This work was supported by the King Abdullah University of Science and Technology (KAUST) Office of Sponsored Research (OSR) under Award No. OSR-2018-CARF/CCF-3079. SA and FL are very grateful for the financial support for conducting the research. CEP acknowledges support by KAUST Global Fellowship Program under Award No. ORA-2022-5002. P.M.-B. acknowledges financial support from Deutsche Forschungsgemeinschaft (DFG, German Research Foundation) under Germany's Excellence Strategy—EXC 2089/1—390776260 (e-conversion) and from TUM.solar in the context of the Bavarian Collaborative Research Project Solar Technologies Go Hybrid (SolTech). X.J. acknowledges the financial support from the Chinese Scholarship Council (CSC). V.N. and T.V. acknowledge the support by the Scientific Grant Agency VEGA, project no. 2/0165/22. **The authors are grateful to Prof. Thuc-Quyen Nguyen, University of California, Santa Barbara, for valuable discussion during the revision of the manuscript.**

## References

- [1] F. Liu *et al.*, "Organic Solar Cells with 18% Efficiency Enabled by an Alloy Acceptor: A Two-in-One Strategy," (in English), *Adv. Mater.*, Article vol. 33, no. 27, p. 8, Jul 2021, Art no. 2100830, doi: 10.1002/adma.202100830.
- [2] M. B. Salim, R. Nekovei, and R. Jeyakumar, "Organic tandem solar cells with 18.6% efficiency," (in English), *Sol. Energy*, Article vol. 198, pp. 160-166, Mar 2020, doi: 10.1016/j.solener.2020.01.042.
- [3] K. Jin, Z. Xiao, and L. Ding, "18.69% PCE from organic solar cells," *Journal of Semiconductors*, vol. 42, no. 6, p. 060502, 2021/06/01 2021, doi: 10.1088/1674-4926/42/6/060502.
- [4] Z.-C. Wen, H. Yin, X.-T. J. S. Hao, and Interfaces, "Recent progress of PM6: Y6-based high efficiency organic solar cells," vol. 23, p. 100921, 2021.
- [5] Y. Lin *et al.*, "A simple n-dopant derived from diquat boosts the efficiency of organic solar cells to 18.3%," vol. 5, no. 12, pp. 3663-3671, 2020.
- [6] X. Wang, C. X. Zhao, G. Xu, Z.-K. Chen, and F. Zhu, "Degradation mechanisms in organic solar cells: Localized moisture encroachment and cathode reaction," *Solar Energy Materials and Solar Cells*, vol. 104, pp. 1-6, 2012.
- [7] Y. Zhao *et al.*, "Achieving sustainability of greenhouses by integrating stable semi-transparent organic photovoltaics," *Nature Sustainability*, vol. 6, no. 5, pp. 539-548, 2023.

- [8] Y. Li, G. Xu, C. Cui, and Y. Li, "Flexible and semitransparent organic solar cells," *Advanced Energy Materials*, vol. 8, no. 7, p. 1701791, 2018.
- [9] J. Bergqvist *et al.*, "Asymmetric photocurrent extraction in semitransparent laminated flexible organic solar cells," *npj Flexible Electronics*, vol. 2, no. 1, pp. 1-8, 2018.
- [10] D. H. Shin, C. W. Jang, H. S. Lee, S. W. Seo, and S.-H. Choi, "Semitransparent flexible organic solar cells employing doped-graphene layers as anode and cathode electrodes," *ACS Appl. Mater. Interfaces*, vol. 10, no. 4, pp. 3596-3601, 2018.
- [11] D. Angmo, M. Hösel, and F. C. Krebs, "All solution processing of ITO-free organic solar cell modules directly on barrier foil," *Solar energy materials and solar cells*, vol. 107, pp. 329-336, 2012.
- [12] W. Pan, Y. Han, Z. Wang, Q. Luo, C. Ma, and L. Ding, "Over 1 cm<sup>2</sup> flexible organic solar cells," *Journal of Semiconductors*, vol. 42, no. 5, p. 050301, 2021.
- [13] Y. Wang *et al.*, "Top and bottom electrode optimization enabled high-performance flexible and semi-transparent organic solar cells," *Materials Chemistry Frontiers*, vol. 5, no. 11, pp. 4310-4316, 2021.
- [14] Y.-W. Su, S.-C. Lan, and K.-H. Wei, "Organic photovoltaics," *Materials Today*, vol. 15, no. 12, pp. 554-562, 2012.
- [15] H. C. Wang *et al.*, "Sequential Deposition of Donor and Acceptor Provides High-Performance Semitransparent Organic Photovoltaics Having a Pseudo p-i-n Active Layer Structure," *Advanced Energy Materials*, vol. 11, no. 13, p. 2003576, 2021.
- [16] R. Po, A. Bernardi, A. Calabrese, C. Carbonera, G. Corso, and A. Pellegrino, "From lab to fab: how must the polymer solar cell materials design change?—an industrial perspective," *Energy & Environmental Science*, vol. 7, no. 3, pp. 925-943, 2014.
- [17] F. C. Krebs, J. Fyenbo, and M. Jørgensen, "Product integration of compact roll-to-roll processed polymer solar cell modules: methods and manufacture using flexographic printing, slot-die coating and rotary screen printing," *Journal of Materials Chemistry*, vol. 20, no. 41, pp. 8994-9001, 2010.
- [18] M. Riede, D. Spoltore, and K. Leo, "Organic solar cells—the path to commercial success," *Advanced Energy Materials*, vol. 11, no. 1, p. 2002653, 2021.
- [19] J. Wu *et al.*, "Towards a bright future: The versatile applications of organic solar cells," *Materials Reports: Energy*, vol. 1, no. 4, p. 100062, 2021.
- [20] R. Xue, J. Zhang, Y. Li, and Y. Li, "Organic solar cell materials toward commercialization," *Small*, vol. 14, no. 41, p. 1801793, 2018.
- [21] W. Yang *et al.*, "Balancing the efficiency, stability, and cost potential for organic solar cells via a new figure of merit," *Joule*, vol. 5, no. 5, pp. 1209-1230, 2021.
- [22] A. Seemann *et al.*, "Reversible and irreversible degradation of organic solar cell performance by oxygen," *Sol. Energy*, vol. 85, no. 6, pp. 1238-1249, 2011.
- [23] W. Yang, Y. Yao, and C.-Q. Wu, "Mechanisms of device degradation in organic solar cells: Influence of charge injection at the metal/organic contacts," *Organic Electronics*, vol. 14, no. 8, pp. 1992-2000, 2013.
- [24] T. S. Glen *et al.*, "Dependence on material choice of degradation of organic solar cells following exposure to humid air," *Journal of Polymer Science Part B: Polymer Physics*, vol. 54, no. 2, pp. 216-224, 2016.
- [25] Q. Song *et al.*, "Degradation of small-molecule organic solar cells," *Applied physics letters*, vol. 89, no. 25, p. 251118, 2006.
- [26] W. Greenbank, L. Hirsch, G. Wantz, and S. Chambon, "Interfacial thermal degradation in inverted organic solar cells," *Applied Physics Letters*, vol. 107, no. 26, p. 115\_1, 2015.
- [27] M. Jørgensen, K. Norrman, and F. C. Krebs, "Stability/degradation of polymer solar cells," *Solar energy materials and solar cells*, vol. 92, no. 7, pp. 686-714, 2008.

- [28] Z. Wang *et al.*, "Thermodynamic properties and molecular packing explain performance and processing procedures of three D18: NFA organic solar cells," *Adv. Mater.*, vol. 32, no. 49, p. 2005386, 2020.
- [29] A. Agresti, S. Pescetelli, Y. Busby, and T. Aernouts, "Thermally induced fullerene domain coarsening process in organic solar cells," *IEEE Transactions on Electron Devices*, vol. 66, no. 1, pp. 678-688, 2018.
- [30] Z. Li *et al.*, "Toward improved lifetimes of organic solar cells under thermal stress: Substrate-dependent morphological stability of PCDTBT: PCBM films and devices," *Scientific reports*, vol. 5, no. 1, pp. 1-9, 2015.
- [31] B. Conings *et al.*, "Modeling the temperature induced degradation kinetics of the short circuit current in organic bulk heterojunction solar cells," *Applied Physics Letters*, vol. 96, no. 16, p. 81, 2010.
- [32] S. Alam *et al.*, "Thermally induced degradation of PBDTTT-CT: PCBM based polymer solar cells," *Journal of Physics D: Applied Physics*, vol. 52, no. 47, p. 475501, 2019.
- [33] S. Alam *et al.*, "Disentanglement of degradation mechanisms by analyzing aging dynamics of environmentally friendly processed polymer solar cells," *Energy Technology*, vol. 8, no. 12, p. 2000116, 2020.
- [34] L. Duan *et al.*, "Burn-In Degradation Mechanism Identified for Small Molecular Acceptor-Based High-Efficiency Nonfullerene Organic Solar Cells," *ACS Appl. Mater. Interfaces*, vol. 12, no. 24, pp. 27433-27442, 2020.
- [35] Y. Zhao, Z. Wu, X. Liu, Z. Zhong, R. Zhu, and J. Yu, "Revealing the photo-degradation mechanism of PM6: Y6 based high-efficiency organic solar cells," *Journal of Materials Chemistry C*, vol. 9, no. 39, pp. 13972-13980, 2021.
- [36] R. Meitzner *et al.*, "Impact of P3HT materials properties and layer architecture on OPV device stability," *Solar Energy Materials and Solar Cells*, vol. 202, p. 110151, 2019.
- [37] C. J. Schaffer *et al.*, "A direct evidence of morphological degradation on a nanometer scale in polymer solar cells," *Adv. Mater.*, vol. 25, no. 46, pp. 6760-6764, 2013.
- [38] D. Heinrich *et al.*, "Nanoscale Morphology from Donor-Acceptor Block Copolymers: Formation and Functions," in *Elementary Processes in Organic Photovoltaics*, vol. 272, K. Leo Ed., (Advances in Polymer Science. Berlin: Springer-Verlag Berlin, 2017, pp. 157-191.
- [39] L. Tan *et al.*, "Enhanced long-term and thermal stability of polymer solar cells in air at high humidity with the formation of unusual quantum dot networks," *ACS Appl. Mater. Interfaces*, vol. 9, no. 31, pp. 26257-26267, 2017.
- [40] L. Duan, M. Guli, Y. Zhang, H. Yi, F. Haque, and A. Uddin, "The Air Effect in the Burn-In Thermal Degradation of Nonfullerene Organic Solar Cells," *Energy Technology*, vol. 8, no. 5, p. 1901401, 2020.
- [41] Y. Wang *et al.*, "Recent progress and challenges toward highly stable nonfullerene acceptor-based organic solar cells," *Advanced Energy Materials*, vol. 11, no. 5, p. 2003002, 2021.
- [42] H. Cha and J. Wu, "Understanding what determines the organic solar cell stability," *Joule*, vol. 5, no. 6, pp. 1322-1325, 2021.
- [43] Y. Li, T. Li, and Y. Lin, "Stability: next focus in organic solar cells based on non-fullerene acceptors," *Materials Chemistry Frontiers*, vol. 5, no. 7, pp. 2907-2930, 2021.
- [44] H. W. Cho *et al.*, "Thermally durable nonfullerene acceptor with nonplanar conjugated backbone for high-performance organic solar cells," *Advanced Energy Materials*, vol. 10, no. 12, p. 1903585, 2020.
- [45] T. Kim, J. Choi, H. J. Kim, W. Lee, and B. J. Kim, "Comparative study of thermal stability, morphology, and performance of all-polymer, fullerene-polymer, and ternary blend solar cells based on the same polymer donor," *Macromolecules*, vol. 50, no. 17, pp. 6861-6871, 2017.

- [46] W. Ma, C. Yang, X. Gong, K. Lee, and A. J. Heeger, "Thermally stable, efficient polymer solar cells with nanoscale control of the interpenetrating network morphology," *Advanced functional materials*, vol. 15, no. 10, pp. 1617-1622, 2005.
- [47] X. Du *et al.*, "Unraveling the microstructure-related device stability for polymer solar cells based on nonfullerene small-molecular acceptors," *Adv. Mater.*, vol. 32, no. 16, p. 1908305, 2020.
- [48] B. R. Luginbuhl *et al.*, "Resolving Atomic-Scale Interactions in Nonfullerene Acceptor Organic Solar Cells with Solid-State NMR Spectroscopy, Crystallographic Modelling, and Molecular Dynamics Simulations," *Adv. Mater.*, vol. 34, no. 6, p. 2105943, 2022.
- [49] J. Yuan *et al.*, "Single-junction organic solar cell with over 15% efficiency using fused-ring acceptor with electron-deficient core," *Joule*, vol. 3, no. 4, pp. 1140-1151, 2019.
- [50] Y. Qin *et al.*, "The performance-stability conundrum of BTP-based organic solar cells," *Joule*, vol. 5, no. 8, pp. 2129-2147, 2021.
- [51] J. I. Khan *et al.*, "P3HT Molecular Weight Determines the Performance of P3HT: O-IDTBR Solar Cells," *Solar RRL*, vol. 3, no. 8, p. 1900023, 2019.
- [52] J. I. Khan *et al.*, "Impact of Acceptor Quadrupole Moment on Charge Generation and Recombination in Blends of IDT-Based Non-Fullerene Acceptors with PCE10 as Donor Polymer," *Advanced Energy Materials*, vol. 11, no. 28, p. 2100839, 2021.
- [53] X. Jiang *et al.*, "Revealing Donor–Acceptor Interaction on the Printed Active Layer Morphology and the Formation Kinetics for Nonfullerene Organic Solar Cells at Ambient Conditions," *Advanced Energy Materials*, vol. 12, no. 14, p. 2103977, 2022.
- [54] S. Alam *et al.*, "Uphill and downhill charge generation from charge transfer to charge separated states in organic solar cells," (in English), *Journal of Materials Chemistry C*, Article; Early Access p. 27, 2021, doi: 10.1039/d1tc02351a.
- [55] H. Bässler, D. Kroh, F. Schauer, V. Nádaždy, and A. Köhler, "Mapping the density of states distribution of organic semiconductors by employing energy resolved–Electrochemical impedance spectroscopy," *Advanced Functional Materials*, vol. 31, no. 9, p. 2007738, 2021.
- [56] Y. Li *et al.*, "An n-n Heterojunction Configuration for Efficient Electron Transport in Organic Photovoltaic Devices," *Advanced Functional Materials*, vol. 33, no. 9, p. 2209728, 2023.
- [57] S. Alam *et al.*, "P3HT: PCBM polymer solar cells from a didactic perspective," *Journal of Photonics for Energy*, vol. 12, no. 3, pp. 035501-035501, 2022.
- [58] L. L. Wu, H. D. Zang, Y. C. Hsiao, X. T. Zhang, and B. Hu, "Origin of the fill factor loss in bulk-heterojunction organic solar cells," (in English), *Applied Physics Letters*, Article vol. 104, no. 15, p. 4, Apr 2014, Art no. 153903, doi: 10.1063/1.4871582.
- [59] L. J. A. Koster, V. D. Mihailetschi, R. Ramaker, H. Xie, and P. W. Blom, "Light intensity dependence of open-circuit voltage and short-circuit current of polymer/fullerene solar cells," in *Organic Optoelectronics and Photonics II*, 2006, vol. 6192: SPIE, pp. 457-467.
- [60] A. Sokeng Djoumessi *et al.*, "Improved hole extraction selectivity of polymer solar cells by combining PEDOT: PSS with WO<sub>3</sub>," *Energy Technology*, vol. 9, no. 12, p. 2100474, 2021.
- [61] S. Ryu, N. Y. Ha, Y. H. Ahn, J. Y. Park, and S. Lee, "Light intensity dependence of organic solar cell operation and dominance switching between Shockley-Read-Hall and bimolecular recombination losses," *Scientific Reports*, vol. 11, no. 1, Aug 2021, Art no. 16781, doi: 10.1038/s41598-021-96222-w.
- [62] S. Alam *et al.*, "Organic solar cells based on anthracene-containing PPE-PPVs and non-fullerene acceptors," (in English), *Chem. Pap.*, Article; Proceedings Paper vol. 72, no. 7, pp. 1769-1778, Jul 2018, doi: 10.1007/s11696-018-0466-y.
- [63] A. Zusan *et al.*, "The crucial influence of fullerene phases on photogeneration in organic bulk heterojunction solar cells," *Advanced Energy Materials*, vol. 4, no. 17, p. 1400922, 2014.

- [64] B. Yang, Y. Yuan, and J. Huang, "Reduced bimolecular charge recombination loss in thermally annealed bilayer heterojunction photovoltaic devices with large external quantum efficiency and fill factor," *The Journal of Physical Chemistry C*, vol. 118, no. 10, pp. 5196-5202, 2014.
- [65] S. Roland *et al.*, "Fullerene-free polymer solar cells with highly reduced bimolecular recombination and field-independent charge carrier generation," *The journal of physical chemistry letters*, vol. 5, no. 16, pp. 2815-2822, 2014.
- [66] A. Paulke *et al.*, "Charge carrier recombination dynamics in perovskite and polymer solar cells," *Applied Physics Letters*, vol. 108, no. 11, 2016.
- [67] M. Mingeback, S. Walter, V. Dyakonov, and C. Deibel, "Direct and charge transfer state mediated photogeneration in polymer–fullerene bulk heterojunction solar cells," *Applied Physics Letters*, vol. 100, no. 19, 2012.
- [68] J. Kurpiers and D. Neher, "Dispersive non-geminate recombination in an amorphous polymer: fullerene blend," *Scientific reports*, vol. 6, no. 1, p. 26832, 2016.
- [69] J. Kurpiers *et al.*, "Free carrier generation and recombination in PbS quantum dot solar cells," *Applied Physics Letters*, vol. 108, no. 10, 2016.
- [70] J. Kniepert, M. Schubert, J. C. Blakesley, and D. Neher, "Photogeneration and recombination in P3HT/PCBM solar cells probed by time-delayed collection field experiments," *The Journal of Physical Chemistry Letters*, vol. 2, no. 7, pp. 700-705, 2011.
- [71] J. Kniepert, I. Lange, N. J. Van Der Kaap, L. J. A. Koster, and D. Neher, "A conclusive view on charge generation, recombination, and extraction in as-prepared and annealed P3HT: PCBM blends: combined experimental and simulation work," *Advanced Energy Materials*, vol. 4, no. 7, p. 1301401, 2014.
- [72] S. Albrecht *et al.*, "On the field dependence of free charge carrier generation and recombination in blends of PCPDTBT/PC70BM: influence of solvent additives," *The Journal of Physical Chemistry Letters*, vol. 3, no. 5, pp. 640-645, 2012.
- [73] R. Kerremans, C. Kaiser, W. Li, N. Zarrabi, P. Meredith, and A. Armin, "The optical constants of solution-processed semiconductors—new challenges with perovskites and non-fullerene acceptors," *Advanced Optical Materials*, vol. 8, no. 16, p. 2000319, 2020.
- [74] V. Nádaždy, F. Schauer, and K. Gmucová, "Energy resolved electrochemical impedance spectroscopy for electronic structure mapping in organic semiconductors," *Applied Physics Letters*, vol. 105, no. 14, p. 142109, 2014.
- [75] F. Schauer, V. Nádaždy, and K. Gmucová, "Electrochemical impedance spectroscopy for study of electronic structure in disordered organic semiconductors—Possibilities and limitations," *Journal of Applied Physics*, vol. 123, no. 16, p. 161590, 2018.